Thermal Cycling, Microstructure, and Mechanical Properties of Al-Mg-Si-Cu Alloy Bobbin Tool Friction Stir Welded Joints Based on Thermal Index

Yi Li *, Zhigang Zhou, Li Yin *, Dingyao Fu, Haiyi Jiang, Yunxin Yang, Jie Lu and Fuming Jin

School of Mechanical Engineering and Mechanics, Xiangtan University, Xiangtan 411105, China;
202121541981@smail.xtu.edu.cn (Z.Z.); 202021002250@smail.xtu.edu.cn (D.F.); qq2367146052@163.com (H.J.);
202221542197@smail.xtu.edu.cn (Y.Y.); 202221542069@smail.xtu.edu.cn (J.L.); jinfuming0823@163.com (F.J.)
* Correspondence: liyi@xtu.edu.cn (Y.L.); yinli@xtu.edu.cn (L.Y.)

Abstract: The two main process parameters of Bobbin tool friction stir welding (BT-FSW) are ω (rotational speed) and v (traverse speed). Both of these factors have a significant effect on heat input, microstructure, and mechanical properties. At present, most studies on friction stir welding adopt the control variable method to study the thermal cycling during the welding process and the mechanical properties of joints, and there are few studies on changing the two process parameters at the same time, because it can be difficult to assess the correlation between heat input and mechanical properties when changing both factors at the same time. In this study, the w/v ratio is defined as the thermal index, which is a characteristic value of heat input. The study uses ABAQUS 6.5 software to establish a BT-FSW CEL (coupled Eulerian–Lagrangian) thermal coupling model. This model explores the relationship between joint thermal cycles, microstructure, and mechanical properties for different w and v values with the same w/v ratio. The results show that increasing rotational and traverse speeds under the same w/v ratio leads to an increase in the peak temperature of the nugget zone (NZ). However, the peak temperature of the thermo-mechanically affected zone (TMAZ) and heat-affected zone (HAZ) remained almost constant. Joint strength was highest at a rotational speed of 750 r/min and a traverse speed of 650 mm/min, with a yield strength of 227 MPa. As rotational and traverse speeds increased, the recrystallized grain content of the NZ showed an increasing trend followed by a decreasing trend. The recrystallized grain content of the advancing side thermo-mechanically affected zone (AS-TMAZ) and retreating side thermo-mechanically affected zone (RS-TMAZ) showed a decreasing trend. Joint hardness had a "W" shaped distribution, with the highest average hardness value found in the NZ.

Keywords: BT-FSW; thermal cycle; microstructure; mechanical properties

1. Introduction

With the advantages of light weight, good electrical and thermal conductivity, high strength, corrosion resistance and easy processing, aluminum alloys are now widely used in automotive, aerospace and other fields [1–5]. In the application process, the joining method and process parameters are crucial [6]. High-temperature fusion welding can cause defects such as porosity and cracks in the welded joint, which greatly reduces the mechanical properties of the joint [7,8]. BT-FSW is a solid-phase welding method that can effectively avoid the generation of defects such as porosity and cracks. In addition, BT-FSW can also solve problems such as insufficient root welds, ensuring the joint's quality.

Welding quality and welding efficiency are the key issues that must be considered in the application of friction stir welding. The main process parameters for FSW are traverse speed and rotational speed. Ahmed, M.M.Z et al. [9] studied the BT-FSW of a 10 mm thick 1050-H14 aluminum alloy and the effect of various stirring needle shapes and traverse speeds on thermal cycling and weld joint mechanical properties at a constant speed of

600 r/min, with a range of traverse speeds from 200–1000 mm/min; their results show that in the case of using Sq stirring needle, the highest shear strength of the joint obtained at a travel speed of 200 mm/min. Kishan Fuse et al. [10] investigated the effect of different shoulder diameters on a 6 mm thick AA6061-T6 aluminum alloy at traverse speeds of 380 r/min and 31.5 mm/min. The results showed that the size of the defects decreased with increasing traverse speed and good joints were obtained at higher traverse speeds. Jiaxin Chen et al. [11] successfully fabricated 2195-T8 Al-Li alloy FSW joints with different traverse speeds (100–600 mm/min) and constant rotational speed; their results showed that the original T1 precipitates disappeared in the nugget zone (NZ), generating many dislocations. With traverse speeds increasing, joints obtained at lower traverse speeds developed coarser T1 precipitates in the heat-affected zone. Majid Farhang et al. [12] investigated the effect of rotational speed and traverse speed of FSW on residual stresses in aluminum 2024-T6 FSW welds. The results showed that the strain rate has the greatest effect on residual stresses at low rotational speeds; H.J. Liu et al. [13] studied the effect of different shoulder diameters on a 6 mm thick AA6061-T6 aluminum alloy at a constant cooling at 600 r/min speed and the effect of different traverse speeds on the joint properties of 4 mm thick 6061-T6 aluminum alloy; their results showed that when the traverse speed reached 200 mm/min, the tensile strength of the joint reached 69% of that of the base material. Zhang, W. et al. [14] carried out a study on 2198 Al-Cu-Li alloy at a constant rotational speed of 950 r/min and a traverse speed of 90–180 mm/min parameters. Their results showed that when the traverse speed was 150 mm/min, the degree of dynamic recrystallization was high, the isometric crystals were fine, a large number of particles of fine recrystallized phases (β' phase) were diffusely distributed in the NZ zone, and the tensile strength, yield strength, and elongation were 406 MPa, 289 MPa, and 7.2%, respectively.

However, these studies were carried out at low traverse speeds and rotational speeds, where one of the variables was fixed, and very little research has been carried out on the mechanisms by which the different process parameters affect the temperature distribution and microstructure as well as the mechanical properties of the joint.

For stir friction welding, both rotational speed and traverse speed have a significant effect on heat input, microstructure and mechanical properties [15]. However, it is difficult to quantitatively assess the parametric correlation between heat input and mechanical properties when rotational speed and traverse speed are varied simultaneously [16]. Arbegast and Hartley et al. [15] proposed the use of ω^2/v to describe the parametric correlation of heat input during stir friction welding. Ren et al. [17] conducted FSW experiments on a 6 mm thick 6061Al-T651 plate and found that neither the thermal index ω^2/v nor ω/v could be used as a parameter to assess the heat input in FSW. Rajendran C. et al. [18] studied the effect of different ω/v on the mechanical properties of AA2014-T6 aluminum alloy joints, and better-performing joints were obtained when the ratio was 0.33. M. Abbasi Gharacheh et al. [19] studied the effect of different ω/v on the mechanical properties of AZ31 magnesium alloy joints, and the results showed that the joint strength decreased slightly with increasing ω/v. Jamshidi Aval, H. [20] investigated the thermo-mechanical issues associated with the dissimilar friction stir welding process of AA6061 and AA5086 aluminum alloys through smoothed-particle hydrodynamics (SPH) simulation and experimental investigations. The results demonstrate that the presented model accurately predicts the thermal history during the friction stir welding process. Furthermore, both simulation and experimental data indicate that when the AA6061 alloy is located on the advancing side, the temperature profile is drawn towards the AA6061 alloy.

Therefore, in this paper, a thermomechanically coupled CEL model was developed using ABAQUS software to study the joint temperature distribution pattern when the rotational speed and traverse speed were varied simultaneously at a constant ω/v ratio. Subsequently, the BT-FSW of the Al-Mg-Si-Cu alloy with a thickness of 5 mm was carried out to study the effect of temperature distribution, microstructure and mechanical properties of the joint when the rotational speed and traverse speed were varied simultaneously.

2. Materials and Methods

2.1. Finite Element Simulation Model

The CEL method is used to establish a BT-FSW thermo-mechanical coupling model. This method can express the movement of the material in the mesh and can impose precise boundary conditions [21], because in the welding process, the material will undergo a lot of plastic deformation. The use of this method can effectively solve the problem of mesh distortion. In order to improve the computational accuracy and efficiency, a C3D8RT cell grid was used, refining the weld area and coarsening away from the weld area, with the model and mesh subdivision scheme shown in Figure 1. Thermo-physical and mechanical properties of the parent materials versus temperature are shown in Tables 1 and 2. The model contains a total of 1,351,093 hexahedral elements and 1,610,810 nodes.
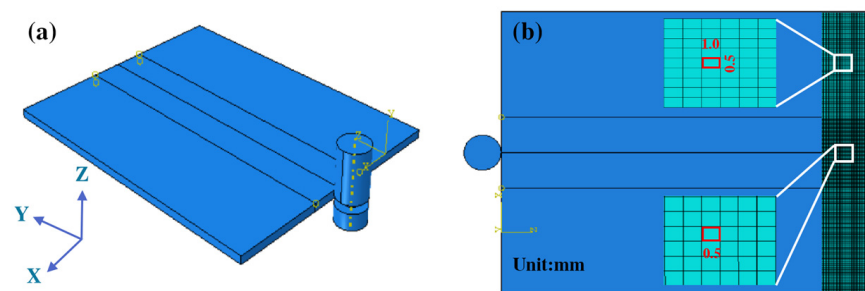
Figure 1. Finite element model. (**a**) Geometric model. (**b**) Grid Segmentation.
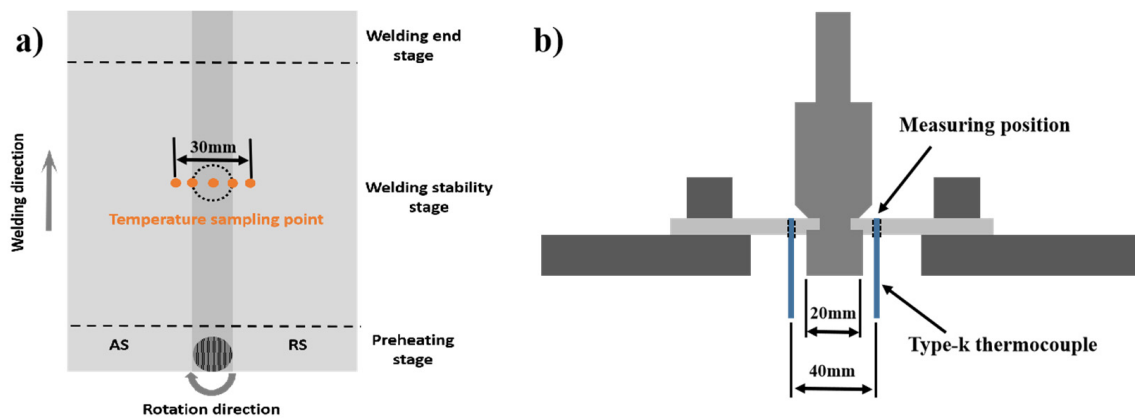
Table 1. Al-Mg-Si-Cu alloy material properties.

Temperature/°C	Density/kg/m^3	Conductivity/W·(m·°C)$^{-1}$	Specific Heat Capacity/J·(kg·°C)$^{-1}$	Thermal Expansion/°C^{-1}
25	2640	118	924	--
50	2630	125	944	--
100	2610	132	954	2.65×10^{-5}
150	2600	139	984	--
200	2600	149	1004	2.75×10^{-5}
250	2640	153	1014	--
300	2590	153	1024	2.88×10^{-5}
350	2590	160	1074	--
400	--	160	--	2.99×10^{-5}
527	--	188	--	3.35×10^{-5}
600	--	--	--	--

Table 2. Al-Mg-Si-Cu alloy J-C model.

Jorhson Cook	A	B	n	m	Melting Point	Transition Temp
Model	281	244	0.42	1.34	586	25

In this model, the penalty function method is used to define the contact face-to-face, and a total of six contact pairs are set between the stirring pin and the side of the plate, the upper and lower shoulders, and the top and bottom of the plate, respectively. Considering the constraint effect of the fixture in the actual welding process, the direction constraint is set on the direction of x, y and z of the plate. Due to the contact between the upper surface of the plate and the fixture, the convective heat transfer coefficient is set to 2000 W/m^2.K, and the other region's convective heat transfer coefficient is set to 20 W/m^2.K [22]. The selection of nodes during simulation and the schematic view of the thermocouple's positions are shown in Figure 2.

Figure 2. (**a**) Selection of nodes. (**b**) Schematic view of the thermocouple's positions.

2.2. Experimental Procedures

The material used in this paper is a $200 \times 80 \times 5$ mm Al-Mg-Si-Cu alloy plate. The base material composition and properties are shown in Tables 3 and 4. The welding was completed by taking side access to the plate, and the weld was fixed in place by means of a mechanical fixture, with the welding direction perpendicular to the rolling direction. The experimental equipment and platform are shown in Figure 3. The welding process parameters developed are shown in Table 5. Chaolei Liu et al. [23] conducted several BT-FSW tests of 6061-T6 at a rotation speed of 400 rpm and traverse speed of 350 mm/min process parameters, allowing them to obtain better performance joints. The ratio of the two was approximately 1.14, so in this paper, the ω/v ratio is assumed to be approximately 1.14, where the amount of downward pressure and tilt angle are 0.1 mm and 0°, respectively. Considering the vibration during the actual welding process, a K-type thermocouple was inserted at a distance from the center of the weld seam for experimental verification. After the end of welding using wire cutting perpendicular to the welding direction to intercept the metallographic specimen, by sandpaper rough grinding, fine grinding, and polishing machine polishing, Keller reagent was used for corrosion of metallographic specimens, with a corrosion time of about 4 min. The microstructure was observed and analyzed using a Zeikang CK-500 optical microscope. The electron backscatter diffraction (EBSD) technique was used to characterize the microstructure of the welds in a day-stand emission scanning electron microscope. Electrolytic polishing was carried out using a solution consisting of 10% $HClO_4$ + 90% C_2H_5OH at 20 V with a current not exceeding 2 A. The scanning step was 1 μm, where grain boundaries with an orientation angle of 2–15° were classified as low-angle grain boundaries (LAGBS) and those larger than 15° as high-angle grain boundaries (HAGBS). The average grain size and grain boundary fraction were calculated by the OIM 7.0 software. Microhardness was measured along the centreline in the thickness direction of the weld cross-section with a load and dwell time of 200 g and 10 s. Specimens for tensile testing were prepared in accordance with GB/T 228-2002 and their geometry, position, and dimensions are shown in Figure 4. The tensile strength of the welded specimens was assessed on the WANCE tensile machine at a loading rate of 2 mm/min at room temperature, and three specimens were tested in each welding condition.

Table 3. Chemical composition of Al-Mg-Si-Cu alloy (wt%).

Al	Mg	Si	Fe	Zn	Cu	Mn	Cr
al	1.07	0.58	0.32	0.05	0.24	0.1	1.82

Table 4. Mechanical properties of Al-Mg-Si-Cu alloy (measured).

Tensile Strength/MPa	Yield Strength/MPa	Elongation Rate/%
281	244	11.84
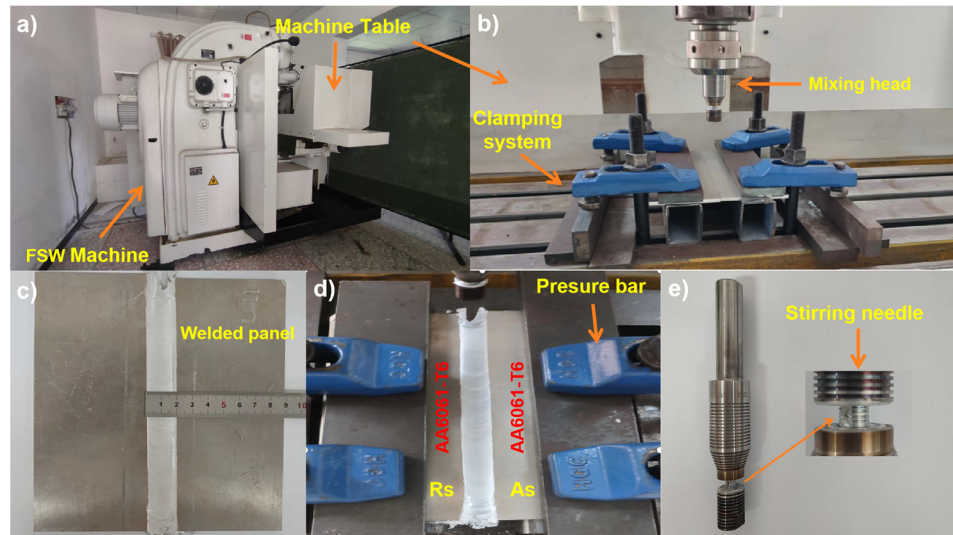
Figure 3. Schematic diagram of experimental equipment and platform: (**a**) FSW equipment; (**b**) experimental platform; (**c**) welded panel; (**d**) welding and clamping; (**e**) mixing head.

Table 5. Experimental parameters for BT-FSW Al-Mg-Si-Cu alloy plate.

NO.	Rotational Speed/(r·min⁻¹)	Traverse Speed/(mm·min⁻¹)	ω/v
1	375	330	1.14
2	475	415	1.14
3	600	525	1.14
4	750	660	1.14
5	950	830	1.14
6	1180	1035	1.14
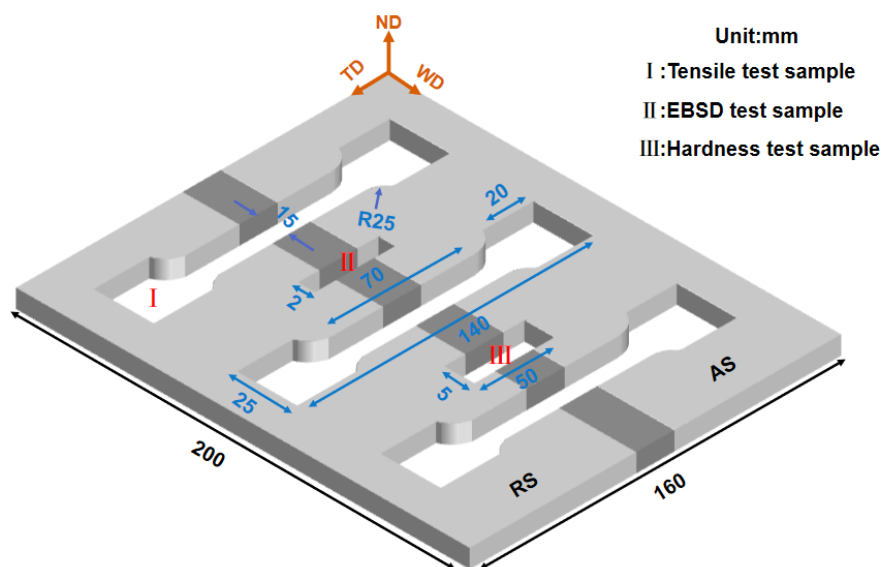
Figure 4. Schematic diagram of tensile specimen and metallographic specimen.

3. Results

3.1. Thermal Cycles

During the BT-FSW process, the welded plate undergoes severe plastic deformation as well as rapid heating and cooling processes. Therefore, the temperature distribution has an important influence on the microstructure and mechanical properties of the joint. Figure 5 shows a cloud plot of the thermal cycles during the stabilization phase with different parameters. The heat source is elliptical in shape and the peak temperature at the center of the weld shows an increasing trend with the increase in traverse speed and rotational speed. Arturo Abúndez et al. [24] concluded from aging tests on 6061-T6 that the strengthening phase precipitation is better in the temperature range of 150–200 °C. In this paper, we set 180 °C as the threshold temperature and compare the action time above 180 °C at different parameters. The center of the weld and locations 10 mm and 15 mm away from the advancing side (AS) and retreating side (RS) were selected as sampling points for the joint temperature under different parameters. The thermal cycling curves are shown in Figure 6, and the peak temperatures all appear in the NZ, with the temperature on the advancing side (AS) slightly higher than that on the retreating side (RS). This result was in accordance with the study presented by Sharghi et al. [25]. The ω/v thermal index cannot be used as a parameter to evaluate the heat input of FSW, but in BT-FSW, the ω/v thermal index likewise does not reflect the peak temperature during the welding process. However, the peak temperature in the TMAZ and HAZ regions showed less difference in peak temperature when the speed and weld speed were varied simultaneously under the same ω/v thermal index. Therefore, the ω/v thermal index can be used to evaluate the heat input in the TMAZ and HAZ region's BT-FSW. At the same time, with the increase in the peak temperature of the joint, the action time above 180 °C gradually becomes shorter. In Figure 7, both the simulation and measurement results are displayed. The temperature error between the actual and simulated temperature at a position 20 mm from the weld center is approximately 15%. This indicates that the simulation results are basically consistent with the actual results.
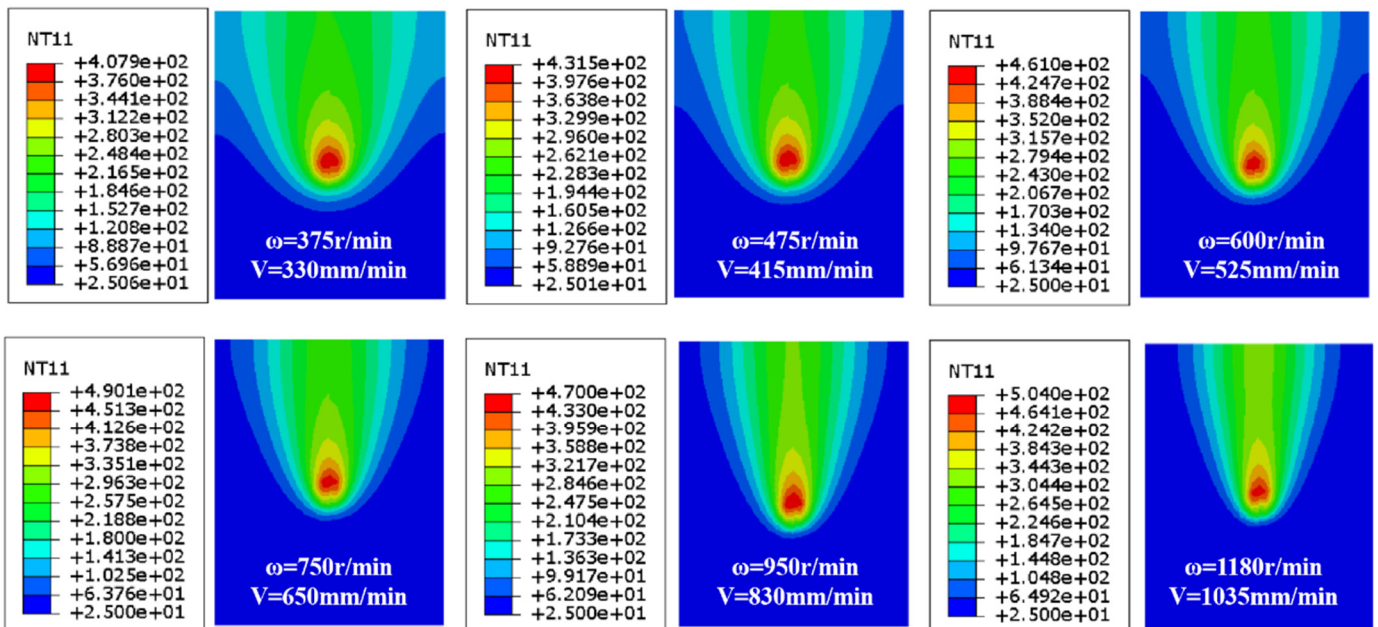

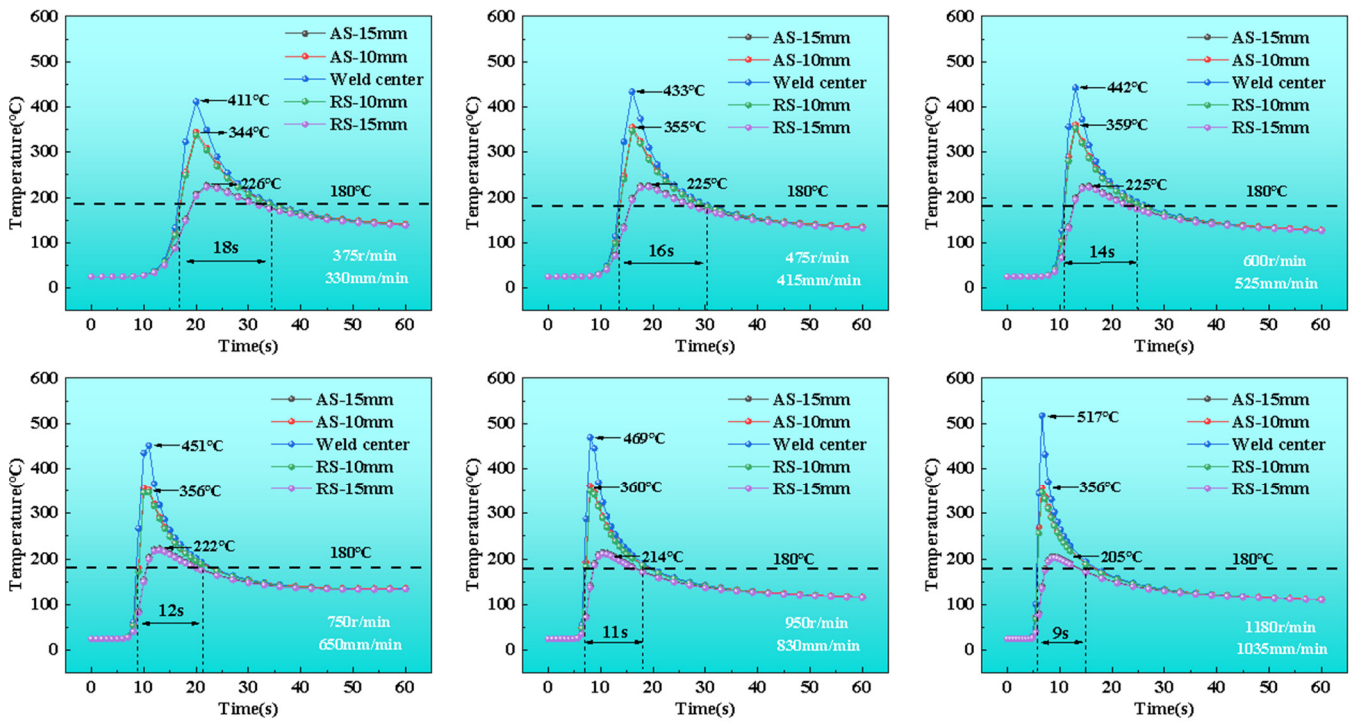**Figure 5.** Cloud map of weld stabilization temperature distribution.

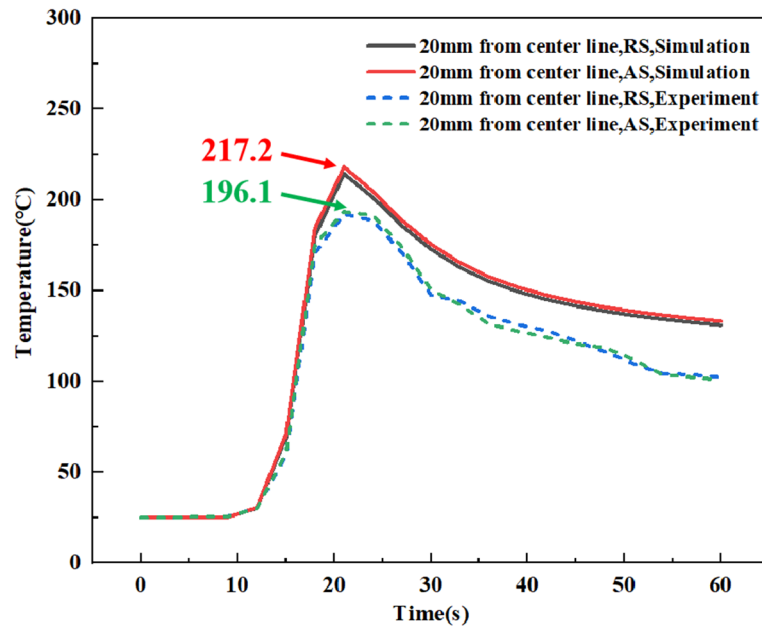**Figure 6.** Joint's thermal cycling curves.

**Figure 7.** Comparing experiment and simulation results of the thermal cycles.

3.2. Macro- and Microstructure

Figure 8 shows the morphology of the welds under different process parameters. It can be seen that all obtain the increase in rotational speed and traverse speed well, all without obvious flying edge generation. The gap of the weld pattern gradually becomes smaller with the increase in rotational speed and traverse speed, part of the weld pattern paste; this is due to the increase in rotational speed, which leads to increased heat input, meaning that the material of the contact surface attachment will be softened.
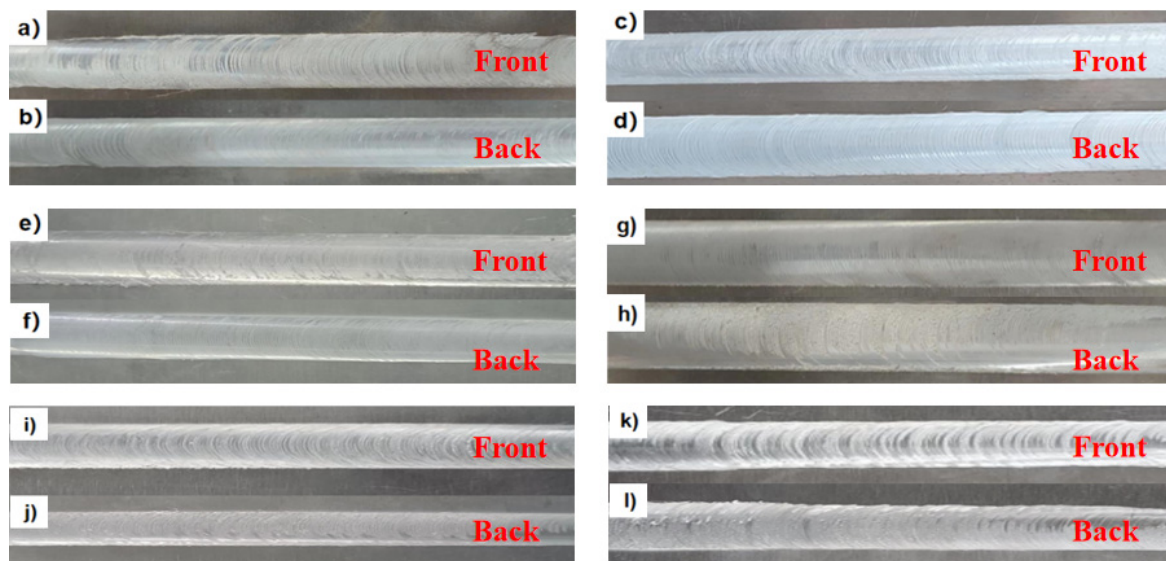
Figure 8. Surface morphologies of weld under different process parameters. (**a**) 375 r/min–330 mm/min front; (**b**) 375 r/min–330 mm/min back; (**c**) 475 r/min–415 mm/min front; (**d**) 475 r/min–415 mm/min back; (**e**) 600 r/min–525 mm/min front; (**f**) 600 r/min–525 mm/min back; (**g**) 750 r/min–650 mm/min front; (**h**) 750 r/min–650 mm/min back; (**i**) 950 r/min–830 mm/min front; (**j**) 950 r/min–830 mm/min back; (**k**) 1180 r/min–1035 mm/min front; (**l**) 1180 r/min–1035 mm/min back.

This article selected three different groups of parameters for EBSD test analysis: 375 r/min–330 mm/min, 475 r/min–415 mm/min, and 750 r/min–650 mm/min. Figure 9 is the microstructure diagram of the weld. The diagram highlights three points (I, II, III) located at AS-TMAZ, NZ, and RS-TMAZ of the weld, respectively. These three points also serve as sampling points for the EBSD samples analyzed in this paper. Due to the EBSD test analysis area being more refined, in order to better compare different rotational speed and traverse speed grain orientation and type, each specimen sampling point location is maintained as consistent as possible. Figure 10 shows the three groups of different welding process parameters. The areas represented from left to right are the AS-TMAZ, NZ, and the RS-TMAZ, respectively. It can be seen that with the increase in rotational speed and traverse speed, the grain size shows an increasing trend. When the rotational speed is 750 r/min and the traverse speed is 650 mm/min, the advancing and retreating sides of the thermo-mechanically affected zone grains appear to have abnormal growth phenomena.
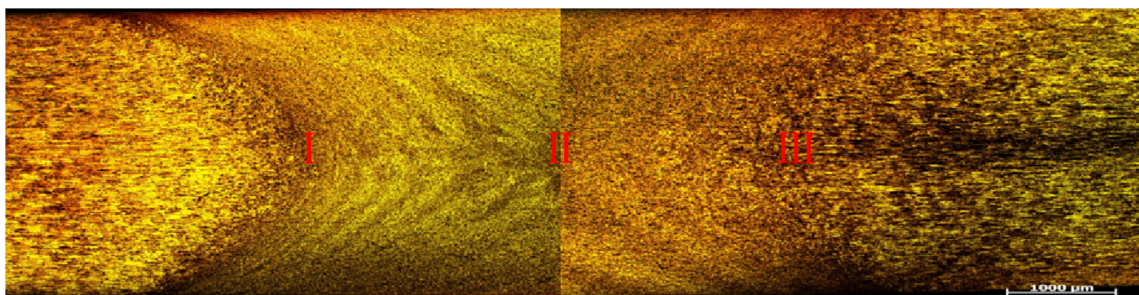
Figure 9. Schematic diagram of EBSD sampling points: (I) AS-TMAZ;(II) NZ; (III) RS-TMAZ.
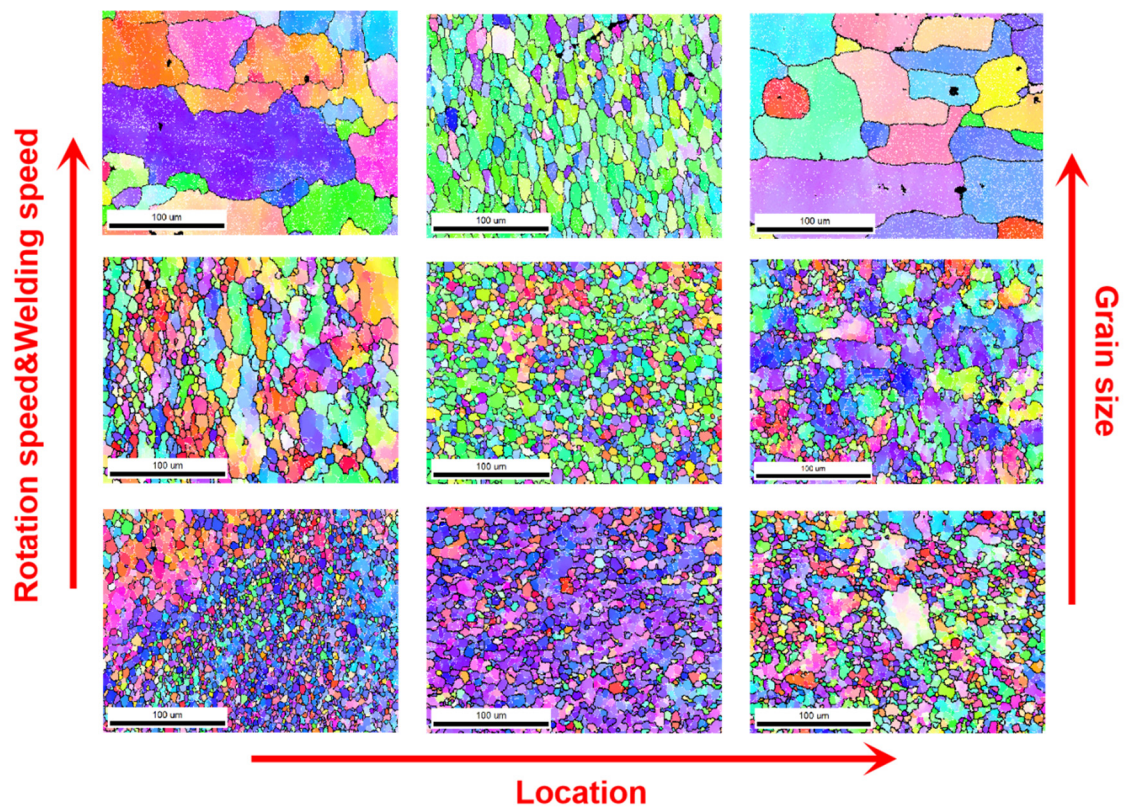
Figure 10. Grain orientation and size diagram at different rotational and traverse speeds.

Preliminary analysis suggests that as the speed increases, the heat input to the weld increases. At the same time, the increase in traverse speed reduces the plastic fluidity of the weld and the nucleation rate; the combined effect of the two leads to a trend of increasing grain size. In the role of higher rotation speed and traverse speed, the weld center temperature may reach the solid solution temperature of aluminum alloy, so that the Mg_2Si reinforcing term particles dissolved in the α-Al matrix and the nucleation effect on the grain boundaries is weakened, resulting in abnormal grain growth in the welding process. According to the research of Rathinasuriyan et al. [26], excessive welding heat input in friction stir welding leads to turbulent flow in the weld fusion zone, thus promoting the formation of defects. Figure 11 shows different rotation speeds and traverse speeds under the influence of grain boundary content. It can be seen that the low-angle grain boundary content shows an increasing trend, and the advancing side of the low-angle grain boundary content value is lower than the retreating side of the low-angle grain boundary content value. When the rotational speed is 750 r/min and the traverse speed is 650 mm/min, the advancing side of the low-angle grain boundary content reaches 55.7%, and the retreating side of the low-angle grain boundary content reaches 75.4%.

Figures 12–14 show the advancing side of the thermo-mechanically affected zone, the nugget zone, and the retreating side of the thermo-mechanically affected zone in different types of grain content for different rotation speeds and traverse speeds. In the advancing side of the thermo-mechanically affected zone, with the increase in rotation speed and traverse speed, recrystallization grain content shows a decreasing trend, and sub-crystallization and deformation grain content shows an increasing trend; in the nugget zone, recrystallization grain content appears to first increase and then decrease. On the contrary, sub-crystallization and deformation grain content first decreases and then increases; in the retreating side of the thermo-mechanically affected zone, recrystallization grain content shows a decreasing trend, and the content of sub-crystallization and deformed grains showed an increasing trend. These results indicate that the increase in rotational speed due

to the increase in temperature promotes dynamic recrystallization to some extent. However, the high temperature caused by too high a rotational speed inhibits the accumulation of dislocations and reduces the driving force of dynamic recrystallization. The thermo-mechanically affected zone is far from the nugget zone, and the stirring needle mechanical stirring effect is very small, mainly because of the upper and lower shoulder extrusion and temperature coupling, so the degree of grain deformation in this region is relatively large. With the increase in rotational speed and traverse speed, and dislocations due to deformation into the low-angle grain boundary, the regional temperature cooling rate also increases with the increase in traverse speed; when the low-angle grain boundary is too late to complete the transformation into high-angle grain boundary, there is a high content of low-angle grain boundary.
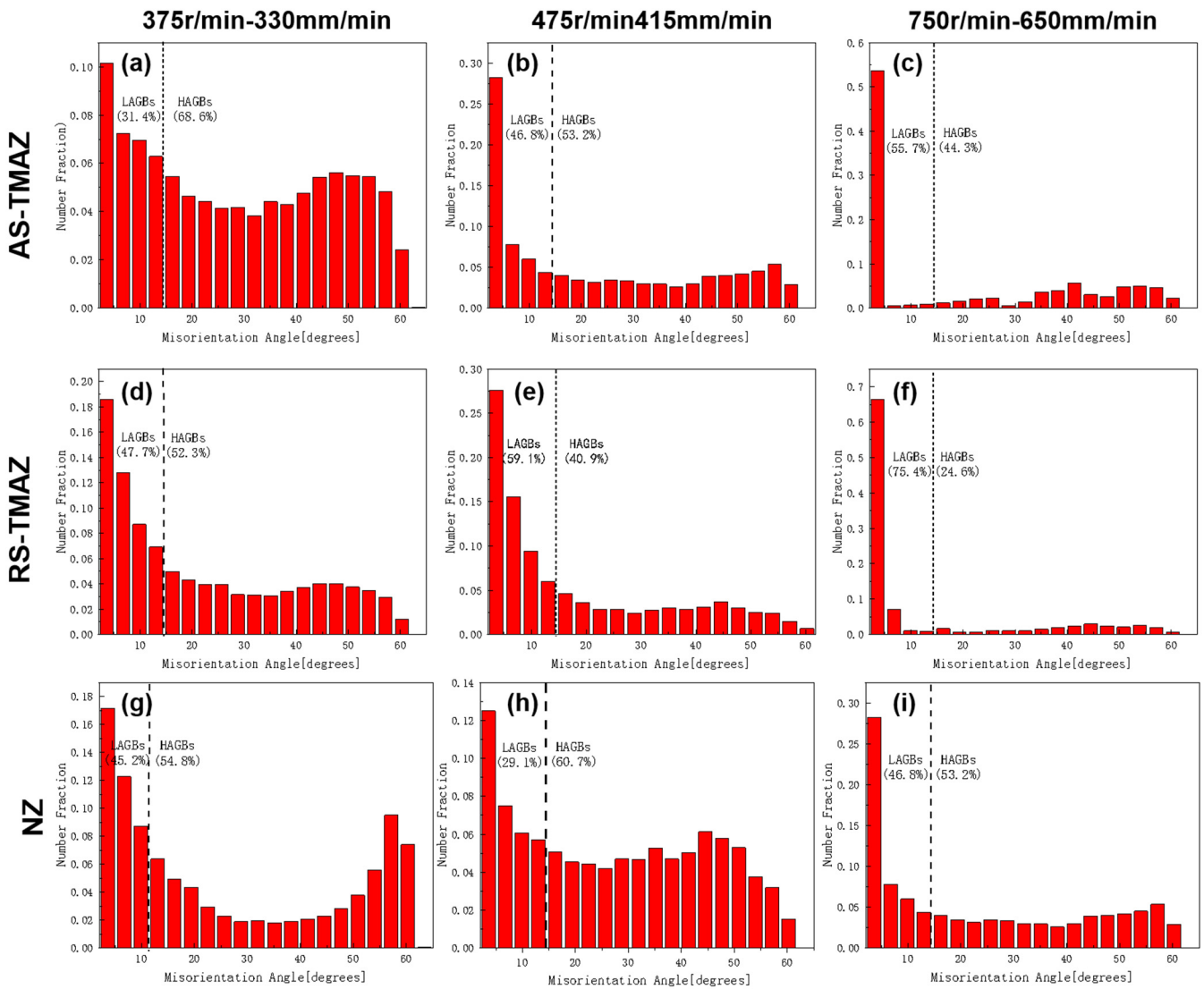

Figure 11. Comparison diagram of grain boundary angle content: (**a**) AS-TMAZ, 375 r/min–330 mm/min; (**b**) AS-TMAZ, 475 r/min–415 mm/min; (**c**) AS-TMAZ, 750 r/min–650 mm/min; (**d**) RS-TMAZ, 375 r/min–330 mm/min; (**e**) RS-TMAZ, 470 r/min–415 mm/min; (**f**) RS-TMAZ, 750 r/min–650 mm/min; (**g**) NZ, 375 r/min–330 mm/min; (**h**) NZ, 475 r/min–415 mm/min; (**i**) NZ, 750 r/min–650 mm/min.
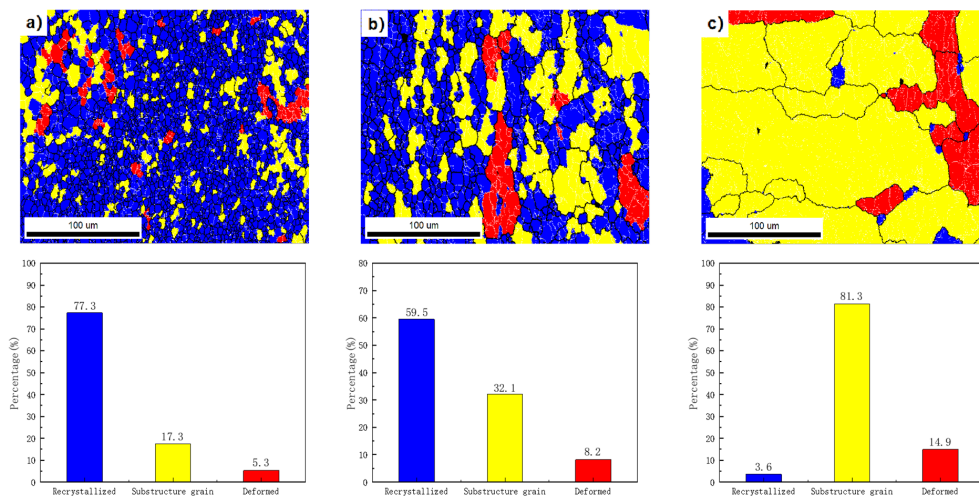
Figure 12. Grain types in the AS-TMAZ under different welding parameters: (**a**) 375 r/min–330 mm/min; (**b**) 475 r/min–415 mm/min; (**c**) 750 r/min–650 mm/min.
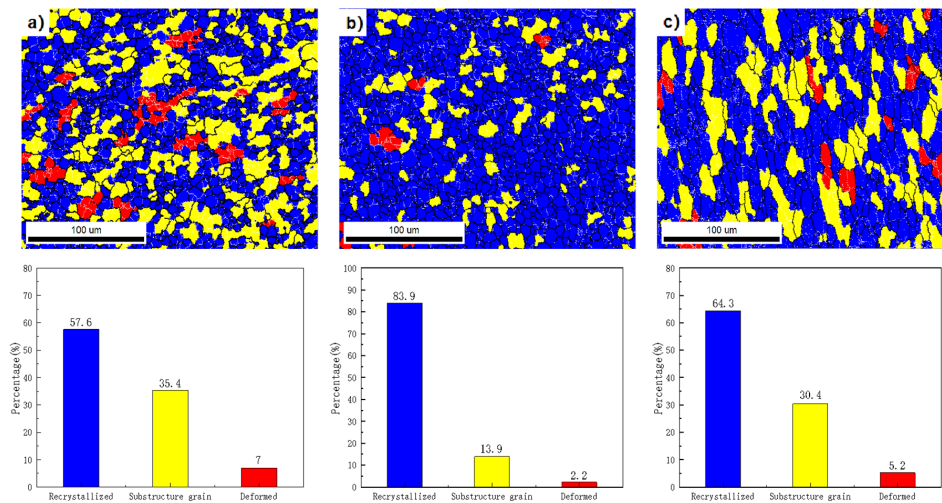
Figure 13. Grain types in the NZ under different welding parameters: (**a**) 375 r/min–330 mm/min; (**b**) 475 r/min–415 mm/min; (**c**) 750 r/min–650 mm/min.
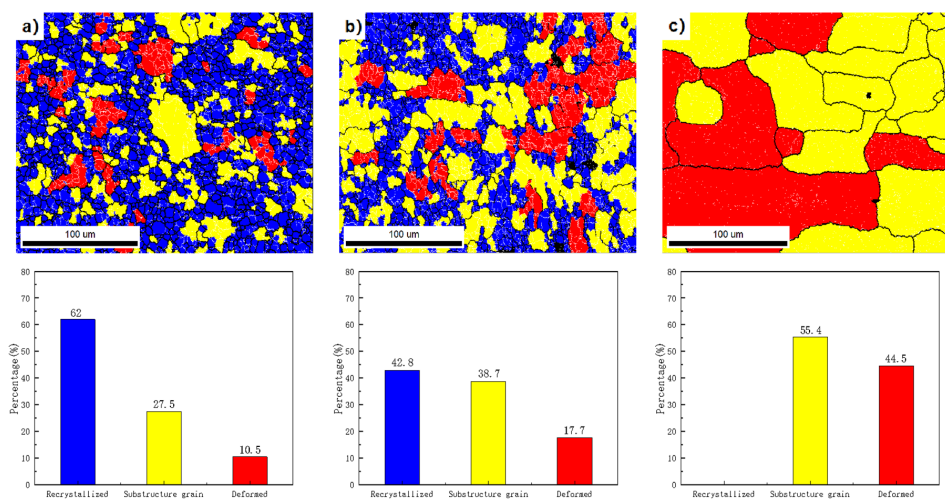
Figure 14. Grain types in the RS-TMAZ under different welding parameters: (**a**) 375 r/min–330 mm/min; (**b**) 475 r/min–415 mm/min; (**c**) 750 r/min–650 mm/min.

3.3. Mechanical Properties

The microhardness distribution along the thickness centerline of the joint cross-section is shown in Figure 15; the overall hardness is a "W" distribution—a roughly symmetrical distribution along the centerline—and the hardness value of the nugget zone from the advancing side to the retreating side slightly decreases, which is caused by the uneven temperature distribution between the advancing side and the retreating side during the actual welding process. The hardness data of Li Liu et al. [27] show the uniformly general softening throughout the dynamically recrystallized weld zone and show a very slight variance within the center of the weld zone and from the top to the bottom of the weld. The variation of hardness in different areas is related to microstructure and precipitation phase distribution and size. The nugget zone is mechanically refined by the stirring needle to make the hardness value higher than the heat-affected zone. As the rotating speed and traverse speed increase, grain coarsening occurs. However, the hardness value of 73.69 HV is the highest in the nugget zone under a rotation speed of 750 r/min and a traverse speed of 650 mm/min.
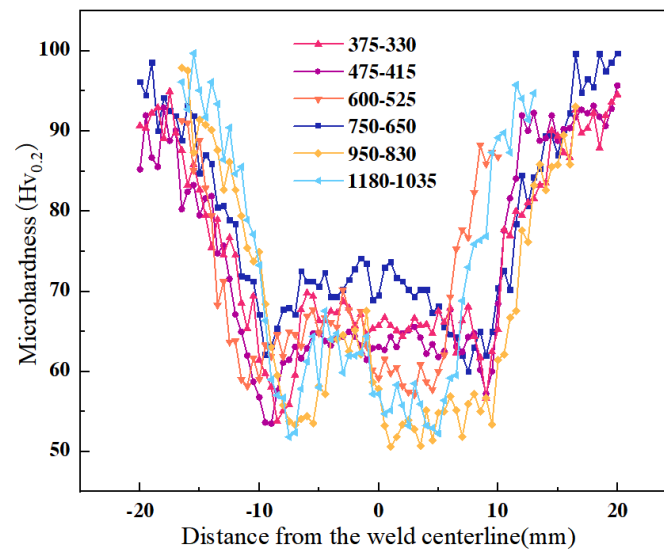

Figure 15. Microhardness profile of joints.

Figure 16 shows the joint strength at different rotation speeds and traverse speeds. Overall, the tensile strength of the joint under all three parameters reached more than 70% of the tensile strength of the parent material. As can be seen in Figure 17, the tensile specimens fractured on the forward side at different rotational and traverse speeds. Therefore, in order to obtain a good quality of the joint under the heat impact factor, increasing or decreasing the rotation speed and traverse speed can obtain a good performance of the joint. Among them, the highest yield strength of the joint under the parameters of rotation speed 750 r/min and traverse speed 650 mm/min is 227 MPa, which is close to the yield strength of the base material. This is due to the parameters of the advancing side and the retreating side of the thermo-mechanically affected zone of the low-angle grain boundary content increasing; thus, dislocation plugging leads to increased grain deformation resistance, so the yield strength is the highest. This finding is in agreement with Jeong-Won Choi et al. [28]. The main strengthening mechanisms in this study are also grain boundary strengthening and dislocation strengthening. At the same time, the content of low-angle grain boundaries in the thermo-mechanically affected zone on the retreating side is generally higher than that on the advancing side, which is one of the main reasons why the tensile specimens all fracture on the advancing side. It is worth mentioning that Kishan Fuse and Won-Bae Lee et al. [29,30] experimentally derived the maximum values of the strength of friction stir welded joints of 6061 aluminum alloy as 189.16 MPa and 200 MPa, respectively, while the tensile strength of the joints welded with each of the parameters in this thesis was

around 220 MPa. This indicates that the method used in this study can obtain high-performance joints.
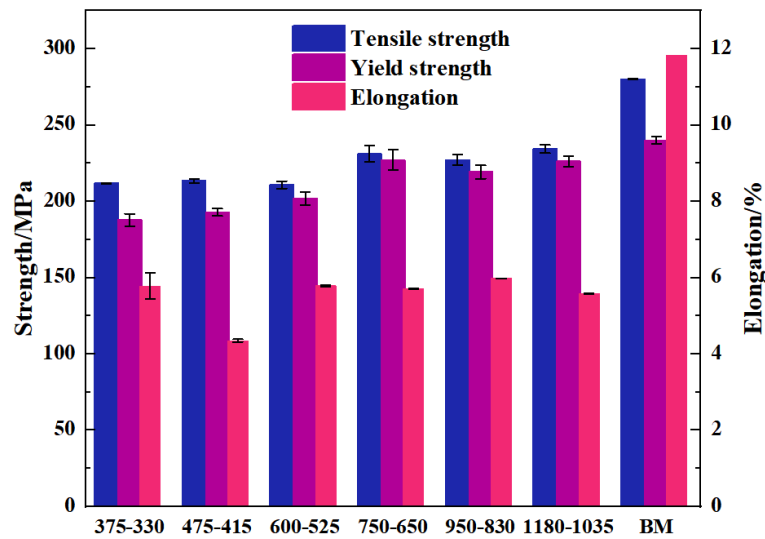

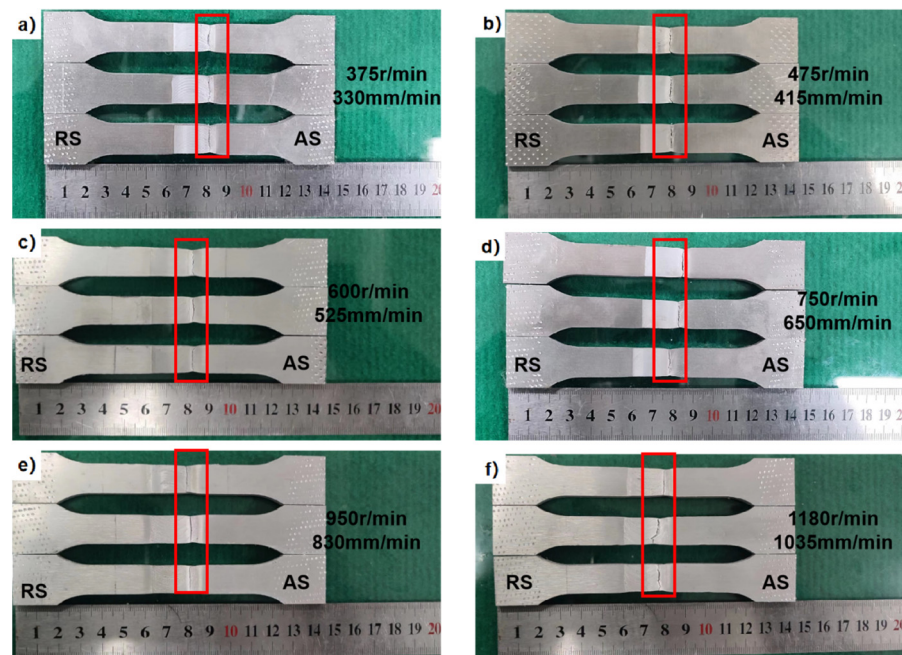**Figure 16.** Tensile properties of the joints.

Figure 17. Tensile specimens at different rotation speeds and traverse speeds. (**a**) 375 r/min–330 mm/min; (**b**) 475 r/min–415 mm/min; (**c**) 600 r/min–525 mm/min; (**d**) 750 r/min–650 mm/min; (**e**) 950 r/min–830 mm/min; (**f**) 1180 r/min–1035 mm/min.

4. Conclusions

In this paper, by studying the effects of different ω and v values on the thermal cycling, microstructure and mechanical properties of joints at the same ω/v, the following conclusions are drawn:

1. The presented model can estimate temperature changes in the BT-FSW of the Al-Mg-Si-Cu alloys with a maximum error of 10.7%. The thermal index is not relevant to the peak joint temperature, but it has some relevance to the peak temperature of TMAZ and HAZ.

2. Equiaxed grains appeared in the NZ due to the dynamic recrystallization behavior, but excessive deformation inhibits recrystallization and thus grain growth
3. The decreasing trend in the content of high-angle grain boundaries in AS-TMAZ and RS-TMAZ is mainly due to dislocation plugging induced by deformation.
4. Good quality joints can be obtained when the thermal index is 1.14, and the tensile strength can reach more than 70% of the strength of the base material.
5. When the rotational speed is 750 r/min and the traverse speed is 650 mm/min, the tensile strength of the joint can reach 231 MPa and the yield strength can reach 227 MPa, which are 82.5% and 92.5% of parent material, respectively.
6. Excessive deformation caused by dislocation plugging, resulting in increased grain deformation resistance, is the main reason for the increase in yield strength of welded joints.

Author Contributions: Conceptualization, Y.L. and D.F.; Methodology, Y.L. and D.F.; Validation, Z.Z. and H.J.; formal analysis, Y.Y. and J.L.; data curation, F.J.; Writing—original draft preparation, Z.Z.; writing—review and editing, Y.L. and L.Y.; supervision, Y.L. and L.Y.; funding acquisition, Y.L. and L.Y. All authors have read and agreed to the published version of the manuscript.

Institutional Review Board Statement: Not applicable.

Informed Consent Statement: Not applicable.

Data Availability Statement: The raw processed data required to reproduce these findings cannot be shared at this time as the data also forms part of an ongoing study.

Conflicts of Interest: The authors declare no conflict of interest.

References

1. Wang, B.; Zhang, Z.; Xu, G.; Zeng, X.; Hu, W.; Matsubae, K. Wrought and cast aluminum flows in China in the context of electric vehicle diffusion and automotive lightweighting. *Resour. Conserv. Recycl.* **2023**, *191*, 106877. [CrossRef]
2. Zhan, H.; Zeng, G.; Wang, Q.; Wang, C.; Wang, P.; Wang, Z.; Xu, Y.; Hess, D.; Crepeau, P.; Wang, J. Unified casting (UniCast) aluminum alloy—A sustainable and low-carbon materials solution for vehicle light-weighting. *J. Mater. Sci. Technol.* **2023**, *154*, 251–268. [CrossRef]
3. Loganathan, K.; Vijaya Siva Subramani, S.K. Design and optimization of aluminium alloy wheel rim in automobile industry. *Mater. Today Proc.* **2023**, *in press*. [CrossRef]
4. Shah, Q.M.Z.; Chowdhury, M.A.; Kowser, M.A. The aspect of the corrosion pitting with fretting fatigue on aluminum alloy: An aerospace structural failure or a nuclear safety phenomenon. *Results Eng.* **2022**, *15*, 100483. [CrossRef]
5. Atxaga, G.; Arroyo, A.; Canflanca, B. Hot stamping of aerospace aluminium alloys: Automotive technologies for the aeronautics industry. *J. Manuf. Process.* **2022**, *81*, 817–827. [CrossRef]
6. Senthil, S.M.; Sradeep, M.; Sharan, K.; Selvapravin, P.A. Flexural and crashworthiness studies of friction stir welded aluminum alloy pipes. *Mater. Today Proc.* **2022**, *50*, 977–980. [CrossRef]
7. Gunda, V.R.; Sanke, N. Evaluation of tensile and microstructure properties of AA2014 and AA7075 FSW weldments developed by HSS-10%Co and WC tools. *Mater. Today Proc.* **2021**, *46*, 913–918.
8. Jacquin, D.; Guillemot, G. A review of microstructural changes occurring during FSW in aluminium alloys and their modelling. *J. Mater. Process. Technol.* **2021**, *288*, 116706. [CrossRef]
9. Ahmed, M.M.Z.; Habba, M.I.A.; El-Sayed Seleman, M.M.; Hajlaoui, K.; Ataya, S.; Latief, F.H.; EL-Nikhaily, A.E. Bobbin Tool Friction Stir Welding of Aluminum Thick Lap Joints: Effect of Process Parameters on Temperature Distribution and Joints' Properties. *Materials* **2021**, *14*, 4585. [CrossRef]
10. Fuse, K.; Badheka, V. Effect of shoulder diameter on bobbin tool friction stir welding of AA 6061-T6 alloy. *Mater. Today Proc.* **2021**, *42*, 810–815. [CrossRef]
11. Chen, J.; Liao, H.; Chen, R.; Tian, Y.; Zhang, Z.; Liu, S.; Song, S. The Correlation of Kissing Bond, Microstructure and Mechanical Properties of the 2195 Al-Li Alloy Friction Stir Welding Joints at Different Welding speeds. *Metals* **2023**, *13*, 1326. [CrossRef]
12. Farhang, M.; Sam-Daliri, O.; Farahani, M.; Vatani, A. Effect of friction stir welding parameters on the residual stress distribution of Al-2024-T6 alloy. *J. Mech. Eng. Sci.* **2021**, *15*, 7684–7694. [CrossRef]
13. Liu, H.; Hou, J.; Guo, H. Effect of welding speed on microstructure and mechanical properties of self-reacting friction stir welded 6061-T6 aluminum alloy. *Mater. Des.* **2013**, *50*, 872–878. [CrossRef]
14. Zhang, W.; Mao, Y.; Yang, P.; Li, N.; Ke, L.; Chen, Y. Effect of Welding Speed on Microstructure Evolution and Mechanical Properties of Friction Stir Welded 2198 Al-Cu-Li Alloy Joints. *Materials* **2022**, *15*, 969. [CrossRef]

15. Ni, Y.; Liu, Y.; Zhang, P.; Huang, J.; Yu, X. Thermal cycles, microstructures and mechanical properties of AA7075-T6 ultrathin sheet joints produced by high speed friction stir welding. *Mater. Charact.* **2022**, *187*, 111873. [CrossRef]
16. Arbegast, W.J.; Hattel, P.J. Friction stir weld technology development at Lockheed Martin Michoud Space System. In Proceedings of the Fifth International Conference on Trends in Welding Research, Pine Mountain, GA, USA, 1–5 June 1998; pp. 541–546.
17. Ren, S.; Ma, Z.; Chen, L. Effect of welding parameters on tensile properties and fracture behavior of friction stir welded Al–Mg–Si alloy. *Scr. Mater.* **2007**, *56*, 69–72. [CrossRef]
18. Rajendran, C.; Abdulriyazdeen, A.; Abishek, S.; Aatheeshwaran, A.; Akash, A. Prediction of relationship between angular velocity to the pitch line velocity (ω/v) on tensile strength of friction stir welded AA2014-T6 Aluminium alloy joints: Angular velocity to pitch line velocity ratio on FSW joints. *Forces Mech.* **2021**, *4*, 100036. [CrossRef]
19. Abbasi Gharacheh, M.; Kokabi, A.H.; Daneshi, G.H.; Shalchi, B.; Sarrafi, R. The influence of the ratio of "rotational speed/traverse speed"(ω/v) on mechanical properties of AZ31 friction stir welds. *Int. J. Mach. Tools Manuf.* **2006**, *46*, 1983–1987. [CrossRef]
20. Aval, H.J. Smoothed-Particle Hydrodynamics (SPH) Simulation of AA6061-AA5086 Dissimilar Friction Stir Welding. *Metals* **2023**, *13*, 906. [CrossRef]
21. Noh, W.F. *CEL: A Time-Dependent, Two-Space-Dimensional, Coupled Eulerian-Lagrange Code*; Methods in Computational Physics; Academic Press: New York, NY, USA, 1964; pp. 117–179.
22. Veljić, D.M.; Perović, M.M.; Sedmak, A.S.; Rakin, M.P.; Trifunović, M.V.; Bajić, N.S.; Bajić, D.R. A coupled thermo-mechanical model of friction stir welding. *Therm. Sci.* **2012**, *16*, 527–534. [CrossRef]
23. Liu, C. *Research on Process and Mechanism of 6061 Aluminum Alloy Double Shoulder Friction Stir Welding*; Harbin Institute of Technology: Harbin, China, 2015.
24. Abúndez, A.; Pereyra, I.; Campillo, B.; Serna, S.; Alcudia, E.; Molina, A.; Blanco, A.; Mayén, J. Improvement of ultimate tensile strength by artificial ageing and retrogression treatment of aluminium alloy 6061. *Mater. Sci. Eng. A* **2016**, *668*, 201–207. [CrossRef]
25. Sharghi, E.; Farzadi, A. Simulation of temperature distribution and heat generation during dissimilar friction stir welding of AA6061 aluminum alloy and Al-Mg2Si composite. *Int. J. Adv. Manuf. Technol.* **2022**, *118*, 3147–3159. [CrossRef]
26. Chandran, R.; Santhanam, S.K.V. Submerged Friction Stir Welding of 6061-T6 Aluminium Alloy under Different Water Heads. *Mater. Res.* **2018**, *21*, e20171070. [CrossRef]
27. Liu, L.; Nakayama, H.; Fukumoto, S.; Yamamoto, A.; Tsubakino, H. Microscopic Observations of Friction Stir Welded 6061 Aluminum Alloy. *Mater. Trans.* **2004**, *45*, 288–291. [CrossRef]
28. Choi, J.-W.; Li, W.; Ushioda, K.; Yamamoto, M.; Fujii, H. Effect of applied pressure on microstructure and mechanical properties of linear friction welded AA1050-H24 and AA5052-H34 joints. *Sci. Technol. Weld. Join.* **2022**, *27*, 92–102. [CrossRef]
29. Fuse, K.; Badheka, V. Hybrid Self-Reacting Friction Stir Welding of AA 6061-T6 Aluminium Alloy with Cooling Assisted Approach. *Metals* **2020**, *11*, 16. [CrossRef]
30. Lee, W.-B.; Yeon, Y.-M.; Jung, S.-B. Mechanical Properties Related to Microstructural Variation of 6061 Al Alloy Joints by Friction Stir Welding. *Mater. Trans.* **2004**, *45*, 1700–1705. [CrossRef]